This is a repository copy of *Structural metamaterial lattices by laser powder-bed fusion of 17-4PH steel*.

White Rose Research Online URL for this paper:
https://eprints.whiterose.ac.uk/206810/

Version: Published Version

Article:
Freeman, F.S.H.B. orcid.org/0000-0002-7402-1790, Jones, L. orcid.org/0000-0001-9927-0913, Goodall, A. et al. (2 more authors) (2024) Structural metamaterial lattices by laser powder-bed fusion of 17-4PH steel. Additive Manufacturing Letters, 8. 100190. ISSN 2772-3690

https://doi.org/10.1016/j.addlet.2023.100190

Reuse
This article is distributed under the terms of the Creative Commons Attribution (CC BY) licence. This licence allows you to distribute, remix, tweak, and build upon the work, even commercially, as long as you credit the authors for the original work. More information and the full terms of the licence here: https://creativecommons.org/licenses/

Takedown
If you consider content in White Rose Research Online to be in breach of UK law, please notify us by emailing eprints@whiterose.ac.uk including the URL of the record and the reason for the withdrawal request.

eprints@whiterose.ac.uk
https://eprints.whiterose.ac.uk/

Additive Manufacturing Letters 8 (2024) 100190

Contents lists available at ScienceDirect

Additive Manufacturing Letters

journal homepage: www.elsevier.com/locate/addlet

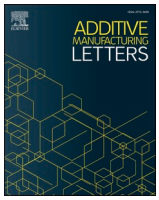

Short Communication

Structural metamaterial lattices by laser powder-bed fusion of 17-4PH steel

Felicity S.H.B. Freeman [a,*], Luke M. Jones [a], Alexander D. Goodall [b], Hassan Ghadbeigi [a], Iain Todd [b]

[a] Department of Mechanical Engineering, University of Sheffield, Sir Frederick Mappin Building, Mappin Street, Sheffield S1 3JD, UK
[b] Department of Materials Science & Engineering, University of Sheffield, UK

ARTICLE INFO

Keywords:
Structural metamaterial
Martensitic transformation
Additive manufacturing
Laser powder bed fusion
Mechanically graded

ABSTRACT

Additive manufacturing build parameters are used to engineer structural metamaterials lattices with controllable mechanical performance, achieved through microstructural grading of 17-4PH steel without compositional or geometric modification. The high solidification rates of laser powder-bed fusion suppress the thermal martensitic transformation and lead to elevated levels of retained austenite. Diamond cubic lattices built at low energy density (low thermal strain) retain a low martensite phase fraction (3 wt%) and exhibit a bend-dominated compression response. Lattices built at high energy density experience increased thermal strain during the build, causing in-situ deformation-driven transformation, yielding 44 wt% martensite; these exhibit a stretch-dominated compression response. Metamaterial lattices, with high and low energy density parameters in different configurations, exhibit mixed compression responses. Controllable mechanical response was achieved through control of microstructure, using build parameters to adjust thermal strain and selectively suppress or trigger the martensitic phase transformation in-situ.

1. Introduction

Manufacturers need highly engineered materials capable of meeting stringent performance requirements, while also being easily recyclable for sustainability. Structural metamaterials are ideally placed to meet this need, applying lessons from Nature to component design by tailoring material response to local requirements. Fabricating these advanced material forms has only recently become achievable with emerging manufacturing technologies, yet they have the potential to transform component design [1,2].

Sustainable manufacturing processes require a composition-sensitive approach, ensuring that material is uncontaminated and value is retained for future recyclability [3]. To this end, it is essential to maximise the potential from existing alloys which are already in common usage and have well established recycling routes. Many of these alloys exhibit phase transformations associated with functional changes which may be exploited for metamaterial behaviour, maximising their potential and increasing sustainability in comparison to compositional grading [4].

Structural lattices are of particular interest for delivering lightweight components with excellent mechanical performance. The behaviour of a particular lattice depends on the combination of material selection, lattice cell geometry, relative density and loading rate [5,6]. Metal additive manufacturing processes have been widely used to create lattices for applications from biomedical implants to crash impact absorption and heat transfer [7–9].

Geometrically graded lattices have been explored elsewhere in the literature. These have investigated modifications to the lattice unit-cell to achieve a tailored mechanical response, but this approach experiences issues associated with maintaining coherency and the impact on relative density, while generating the localised geometry modifications is computationally intensive [1,10–12].

An alternative approach is presented in this work, exploiting the high-resolution spatial control of thermal history, a feature unique to additive manufacturing (AM), to achieve functional grading without compositional or geometric adjustments. This is used to control the extent of thermally and mechanically sensitive solid-state transformation from weaker, more ductile austenite to stronger, more brittle martensite, enabling the design and manufacture of mechanically graded metamaterials.

Previous work has shown that steels which are near-fully martensitic when conventionally processed, like 17-4PH, can exhibit functionally-

* Corresponding author.
E-mail addresses: f.freeman@sheffield.ac.uk (F.S.H.B. Freeman), l.jones@sheffield.ac.uk (L.M. Jones), adgoodall1@sheffield.ac.uk (A.D. Goodall), h.ghadbeigi@sheffield.ac.uk (H. Ghadbeigi), iain.todd@sheffield.ac.uk (I. Todd).

https://doi.org/10.1016/j.addlet.2023.100190
Received 14 September 2023; Received in revised form 3 December 2023; Accepted 12 December 2023
Available online 13 December 2023
2772-3690/© 2023 The Authors. Published by Elsevier B.V. This is an open access article under the CC BY license (http://creativecommons.org/licenses/by/4.0/).

beneficial transformation-driven behaviour when manufactured by Laser Powder Bed Fusion (LPBF) [13,14]. This arises from the fine solidification cell structure, characteristic of LPBF-processed steels, suppressing thermal martensitic transformation on cooling, and causing elevated levels of retained metastable austenite (>99 %). This austenite will readily transform to deformation martensite, either from in-situ strain during the build or from post-build processing, analogous to 'transformation induced plasticity (TRIP)' steels.

2. Material & methods

Builds were carried out on the Aconity Mini laser powder-bed fusion system, which uses a 70 μm diameter Gaussian beam. Two powders with 15–45 μm particle size distributions were compared, a 316 L powder manufactured by Carpenter and nitrogen-atomised GP1 manufactured by EOS; GP1 powder meets the specification for 17-4PH (Table 1) 316 L shows the mechanical response of a non-transforming austenitic material in comparison to the expected controllable variation in martensite phase content in 17-4PH. The comparison also ensures that the mechanical behaviour of 17-4PH is not due to build quality changes such as porosity or grain size because this would also be evident in the 316 L samples.

The selection of build strategies concentrated on the normalised energy density E* (Eq. (1)) and thermal strain parameter ε* (Eq. (2)) [17,18].

$$E^* = \frac{n\,Q}{(2\,V\,L\,r_B)}\,\frac{1}{\rho C_P(T_m - T_0)}\,\frac{r_B}{H} \tag{1}$$

$$\varepsilon^* = \frac{\beta(T_m - T_0)}{E1}\,\frac{t\,V\,w}{\alpha\sqrt{\rho}}\left(\frac{n\,Q}{V}\right)^{3/2} \tag{2}$$

Energy density is a widely used concept in additive manufacturing, although the calculation approach varies across the literature. The 17-4PH material and Aconity Mini machine parameters (n, r_B, ρ, C_P, T_m, T_0) used in these equations are listed in Table 2. The build specific parameters are (Q, V, L, H) are listed in Table 3.

Thermal strain has been assessed using the thermal strain parameter ε*; this is not a quantitative measure of strain, but rather a normalised parameter that enables comparison between build conditions. Here, β is volumetric thermal expansion coefficient, E is elastic modulus, I is second moment of area, t is the characteristic time, w is melt pool length and α is thermal diffusivity.

The characteristic time is defined as the time to travel the length of the track; in this instance, the track length has been taken to be the strut diagonal, which is 1 mm. The second moment of inertia is geometry dependent, however all the lattices have the same nominal geometry, so this has been set to 1. Further, βE and α have all been set to 1 as this is a comparative analysis within a single material type, and not being related back to true strain. With these modifications, the strain parameter equation simplifies to the form shown below.

$$\varepsilon^* = \frac{(T_m - T_0)\,t\,V\,w}{\sqrt{\rho}}\left(\frac{n\,Q}{V}\right)^{3/2} \tag{3}$$

The melt pool length w is more complex, as it depends on the build parameters themselves. It has been estimated from a model using the Eagar equation, reproduced in Appendix C, for a continuously moving Gaussian beam [20]. This includes a number of assumptions, including modelling as a solid rather than a powder, and with no adjustment for the latent heat of melting, but these are judged acceptable for its use here as a relative parameter. The build parameters and their corresponding E* and ε* are shown in Table 3 (fill offset is discussed in Appendix A). Generally, high energy density (E*) is associated with high thermal strain (ε*) which is expected given the construction of their respective equations.

Table 2
Material and machine parameters used for calculation of energy density E* and thermal strain parameter ε*.

Parameter	Symbol	Value	Reference
Absorption efficiency	n	0.65	[19]
Beam radius	r_B	35 μm	Measured on machine during commissioning
Alloy density	ρ	7.75 g cm^{-3}	[16]
Specific heat capacity	C_P	460 J kg^{-1} K^{-1}	[16]
Solidus temperature	T_m	1677 K	[16]
Ambient temperature	T_0	298 K	N/A

The Low E* parameters are based on the default for 316 L stainless steel on the Aconity Mini; 316 L and 17-4PH have similar compositions and thermal material properties, so this is expected to give good build quality. The High E* parameters are based on previous work using 17-4PH on a Renishaw SLM125 system; the Renishaw used a pulsed, rather than continuous, laser beam so the power and travel speed have been adjusted to achieve comparable melt pool dimensions [20].

The melt pool length predicted by the model ranges from 376 μm for the Low E* condition to 590 μm for the High E* condition. It is not possible to calibrate this by analysis of the built components, as the melt pool length cannot be distinguished after solidification. Literature on in-situ synchrotron x-ray imaging of laser powder-bed fusion measured melt pool lengths of 400 μm for a build at 208 W laser power and 200 mm/s travel speed; this used a 100 μm laser spot diameter, which is larger than the 70 μm used in the Aconity Mini, so would be expected to produce a shorter, wider melt pool for the same laser power and travel speed [21].

The selected lattice geometry was diamond cubic, which had a face-centred cubic node distribution, and space group $Fd\bar{3}m$. The Maxwell stability criterion (4), M, classifies this as a bend-dominated geometry ($M < 0$), according to the number of struts, $b = 16$, and nodes, $j = 14$, in the unit cell [6].

$$\mathrm{M} = \mathrm{b} - 3\mathrm{j} + 6 \tag{4}$$

The lattice had a unit cell side length of 5 mm (node centre to node centre). The nodes were 1.2 mm diameter, and the struts were square sectioned with 1 mm across the diagonal. The samples were built as blocks with 5 unit cells in each direction. The bottom nodes were extended downwards by 1.0 mm, to allow for material loss when the parts were removed from the baseplate by EDM. The relative density has been calculated to be 11.4 % from the CAD geometry of the basic unit cell. A render of the unit cell is shown in Fig. 1.

To examine the influence of microstructural grading on mechanical response, a composite-style metamaterial structure was superimposed on the lattices (Fig. 2). The configurations included uniform lattices (A1 & A2), splitting into nodes and struts (B1 & B2), alternating layers (C1 & C2), and vertical pillars with infill (D1 & D2). By volume, the node/strut

Table 1
Powder chemistry for EOS GP1 compared with 17-4PH specification.

(wt%)	C	Cr	Cu	Fe	Mn	Mo	Ni	Nb	P	S	Si
Powder	0.05	15.1	4.0	Bal	0.4	0.1	4.3	0.23	<0.01	<0.01	0.6
17-4PH Specification [16]	0.07 max	15.0–17.5	3.0–5.0	Bal	1.0 max	–	3.0–5.0	0.15–0.45	0.04 max	0.03 max	1.0 max

Table 3
Build parameters for High and Low energy density conditions. The Low E* power, speed, hatch and layer thickness are the default Aconity Mini parameters for 316 L stainless steel. Fill offset is discussed in Appendix A.

	Power Q (W)	Speed V (mm/s)	Hatch H (μm)	Layer L (μm)	Fill Offset (μm)	MP Length w (μm)	E*	ε* x 10^{-3}
Low E*	150	800	80	30	0.00	376	5	0.25
High E*	195	280	30	30	0.15	590	51	2.82

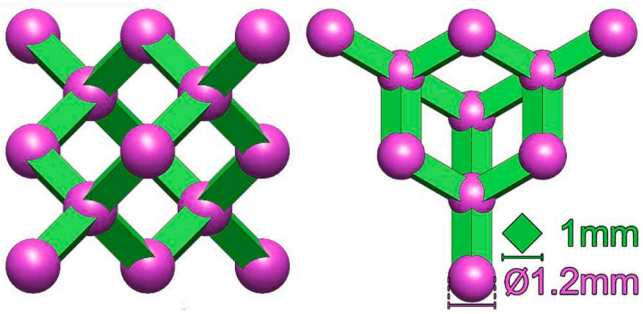

Fig. 1. Unit cell of the 3D printed lattice in front and isometric views.

combinations were 50:50 split, the layered structures were 60:40 split and the pillared structures were 16:84 split. The graded lattices were created with separate CAD models for each parameter set with coincident mating faces.

Quasi-static compression testing was carried out using a crosshead approach speed of 0.5 mm/min. The compression contact area was taken to be 625 mm^2, corresponding to the 25 mm distance between the centres of the spherical corner nodes on the contact surfaces, although strut distortion means this may have increased during the test. Future work will incorporate square end-plates to avoid strut distortion effects.

The initial section of the data, before the stress starts to increase continuously, has been removed from the analysis; this corresponds to any as-built distortion being straightened out and the platen coming into full contact. The sample height has been taken as the distance between the platens at the end of this initial section. The raw data was affected by high frequency noise, so it has been processed through a low-pass filter to remove this and clarify the low frequency signal.

During compression testing, images were captured for 2D digital image correlation (DIC), to track the pattern of displacement through the test. A speckle pattern was applied to the samples for displacement and strain measurement throughout the test. The displacement field is presented here because the local strain of each individual node/strut is low in comparison to the overall strain of the sample. Similar studies presenting strain have used smoothing algorithms, however the displacement field is equally informative without the introduction of errors associated with such smoothing.

3D DIC was investigated for this application to eliminate strain error associated with out of plane displacement, however the highly curved geometry of the struts caused difficulties in achieving a good correlation between the cameras, and 2D DIC was determined to provide acceptable results.

Microstructural characterisation on additively-built 17-4PH has previously been found to be challenging, due to the highly metastable nature of the retained austenite. The cutting and polishing processes used for preparation of samples for both optical and electron microscopy have been demonstrated to cause additional deformation-driven martensitic transformation, reducing their accuracy for determining

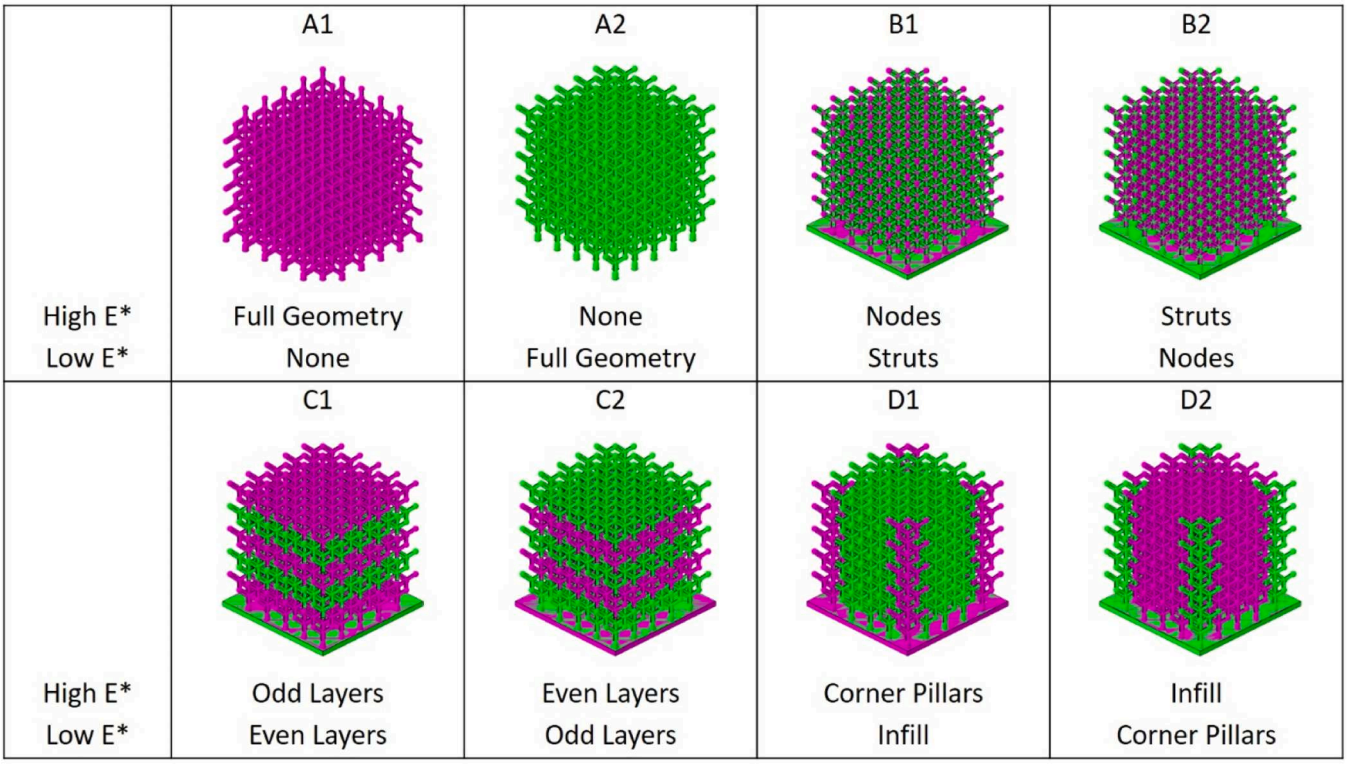

Fig. 2. Sample configurations and built samples of Diamond Cubic lattices. Pink indicates High E* regions, green indicates Low E* regions. Square bases on graded structures were used for alignment between the separate CAD models and were not included in the physical build.

as-built phase fractions of martensite and austenite [14,15].

Phase characterisation has therefore been carried out using a superconducting quantum interference device (SQUID) to determine the saturation magnetisation Ms, following an approach described in the literature and including shape correction for non-spherical samples [13,20,22–24]. SQUID is limited to very small samples (0.01–0.03 g). In preliminary work, test material was harvested from the lattices by cutting off small pieces from the outer faces, but this proved difficult to achieve without causing local deformation, creating new martensite and making the test material unrepresentative of the as-built bulk. To mitigate this, a series of individual 'node + strut' samples were built specifically for SQUID measurement, using just the High E* and Low E* build conditions, and removed from the baseplate with a sharp chisel. This was judged to provide the smallest and most localised deformation zone, minimising the extent of post-build deformation-driven transformation.

3. Results

Fig. 3 shows a selection of the lattice samples before compression testing. The samples all built successfully, with no obvious discontinuities between regions built with different parameters. The High E* parameters produced material which was slightly more reflective than the Low E* material.

Phase characterisation of the 17-4PH material under different build conditions was carried out using SQUID, on individual 'node + strut' samples which had been built specifically for the analysis. The Low E* parameters produced a very low martensite content (3.1 ± 0.5 wt%), while the High E* parameters produced a much higher martensite content (43.7 ± 2.3 wt%). This is consistent with previous work on bulk LPBF 17–4PH [13,14]. Raw data is included in Appendix B, Table 4.

Engineering stress-strain curves for the 17-4PH metamaterial lattices are shown in Fig. 4, with corresponding displacement maps generated by 2D-DIC shown in Fig. 5. The test was performed with a machine wherein the bottom ram moved and the top plate was stationary, therefore the DIC results indicate high displacement at the bottom of the image, approaching 0 mm at the top.

The A1 sample (High E*) had a classic stretch-dominated response with a higher initial yield, followed by post-yield softening as a layer of cells collapses, with this pattern repeating for each layer in the structure sequentially. Conversely, the A2 (Low E*) sample showed a bend-dominated response, with a lower initial yield, followed by a long plateau before densification. The plateau in A2 does have a gradually increasing stress, caused by work hardening. The two structures showed similar elastic responses prior to yield. The displacement field in Fig. 5 shows these two behaviours clearly; the A1 sample having its first two layers collapsed evident from the striations in the displacement magnitude while the A2 sample displays a smooth gradient of displacement. The A2 sample additionally shows barrelling, indicated by the higher magnitude toward the edges at the vertical centre of the sample.

The six metamaterial lattice structures (B1–D2) show combinations of the stretch and bend dominated behaviour exhibited by A1 and A2, although at different phasing and amplitude. This is particularly demonstrated in the DIC image of displacement in sample D1, which shows the effect of the High E* corner pillars surrounding a central Low E* matrix. Sample B1 shows much less barrelling than that of A2 or B2, as evidenced by an equal displacement across each vertical layer, demonstrating that the material properties of the nodes are a dominant factor in the barrelling behaviour.

Engineering stress-strain curves for the 316 L and 17-4PH lattices together are shown in Fig. 6; the 316 L lattices were built for just the A1 (High E*), A2 (Low E*) and B1/B2 (nodes/struts) configurations, and were tested without 2D-DIC. In all cases, the 316 L lattices show a bend-dominated response, with no significant differences between the High E* and Low E* build parameters or the metamaterial configurations.

4. Discussion

Previous work on additively manufactured 17–4PH steel has demonstrated that it is possible to fully stabilise austenite through the use of low energy density (low strain) build parameters, although martensitic transformation can be easily triggered by post-build deformation [14]. The retention of metastable austenite is achieved due to the fine solidification cell structure that arises from the high solidification rates associated with laser powder-bed fusion, which suppresses the thermal martensite start temperature [25,26]. It has also been shown that high energy density (high strain) build parameters drive partial martensitic transformation in-situ, due to the higher thermal strain accrued during the build process. This was previously exploited to enable fabrication of a magnetically graded metamaterial, but it also has the potential to create a mechanically graded metamaterial, without the need for compositional modification.

Literature shows that 17-4PH built with parameters comparable with the low energy density (Low E*) condition used here and no post-build heat treatment produced a material with a yield strength of 570 MPa, which work hardened and achieved 50 % elongation at failure [27]. This material was reported to have 50–75 wt% austenite, although this was based on XRD from a cut and polished surface, so may be an underestimate. Samples were also heat treated; this would recover the dense dislocation walls around the solidification cells, removing the barrier to thermal martensitic transformation on cooling. The heat treated samples showed an increase in yield strength to 857 MPa, with a corresponding reduction in elongation to failure to 7 %. There was no analysis of phase in the heat treated condition, but the increased strength and reduced ductility is characteristic of a higher martensite phase fraction. For comparison, wrought solution-treated 17-4PH has a yield strength of 1103 MPa, elongation to failure of 5 % and is near-fully martensitic [28,29].

Taking this phase-driven change in mechanical performance, and combining it with the ability to control phase through in-situ strain driven by the build parameters, a series of structural metamaterial

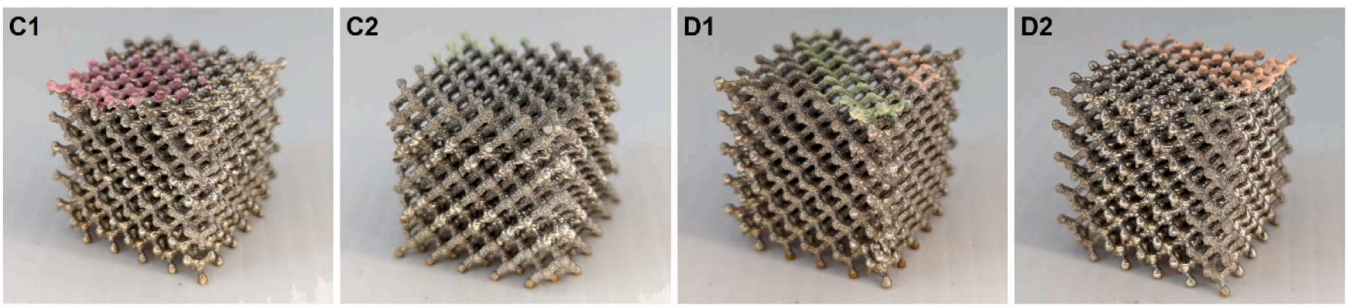

Fig. 3. Lattice samples for metamaterial configurations C1, C2, D1 & D2. Higher energy density regions were slightly more reflective than lower energy density regions. Colours on the top face were for used sample identification during EDM removal from the baseplate.

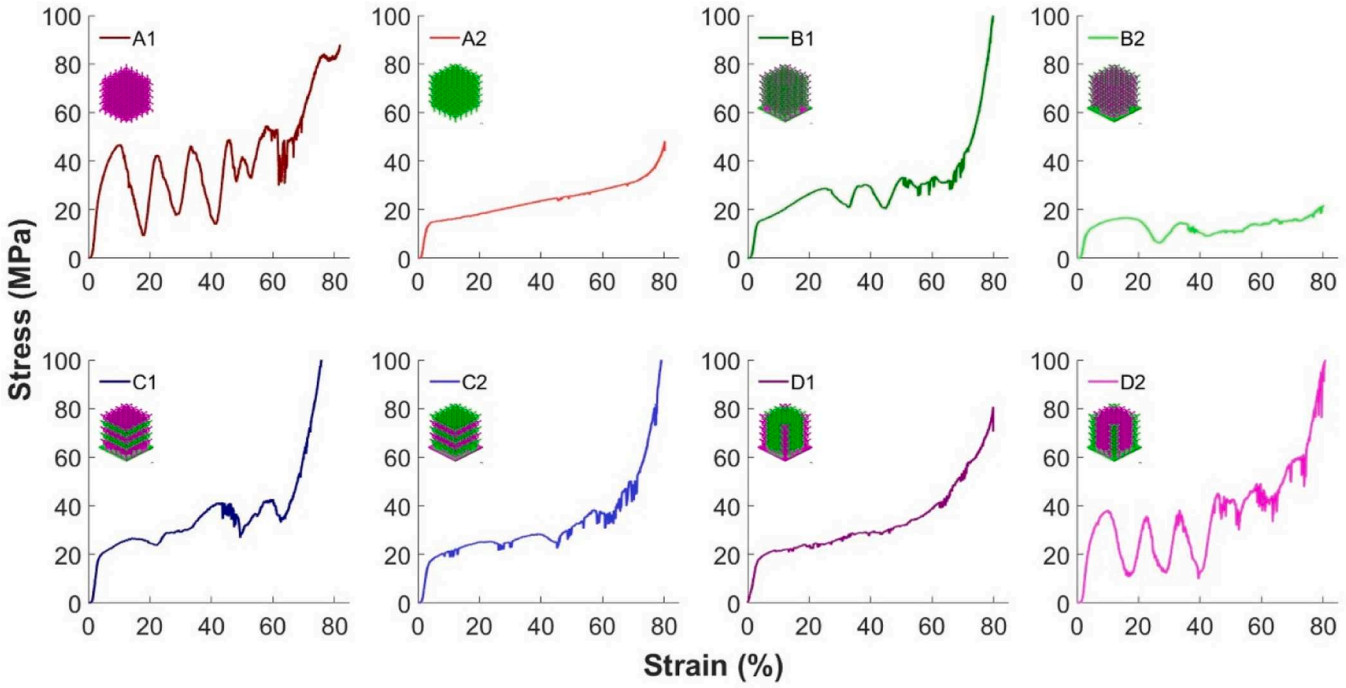

Fig. 4. Stress-strain response for Diamond Cubic lattices built in nitrogen atomised 17–4PH. A1 and A2 were uniform build parameters throughout. B1/B2 were split by nodes & struts. C1/C2 were split by horizontal layers. D1/D2 were split by corner pillars and infill.

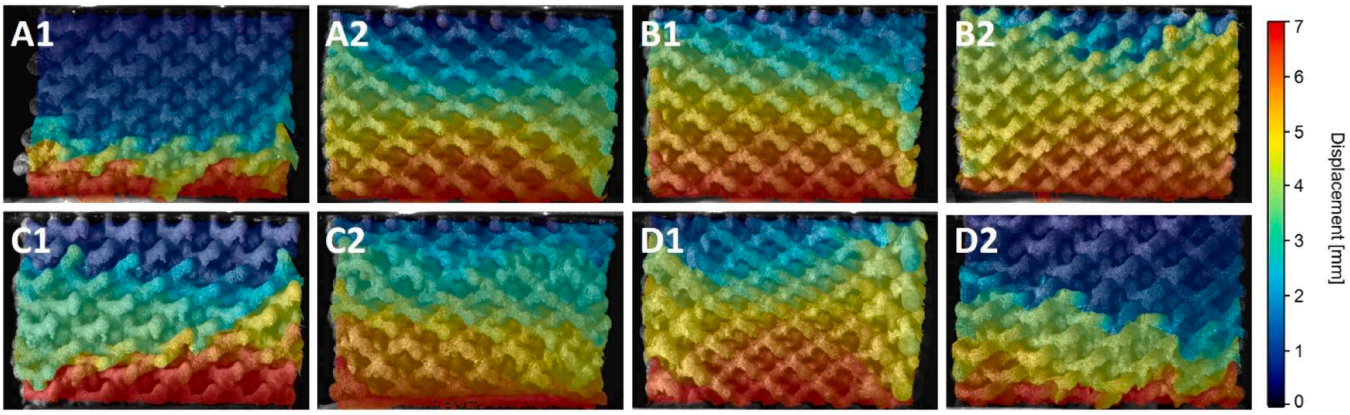

Fig. 5. Displacement after 6 mm of vertical platen movement for Diamond Cubic lattices built in nitrogen atomised 17–4PH, recorded by 2D-DIC. The A1 sample (High E*) shows complete crushing of the bottom layer, with minimal distortion elsewhere. The A2 sample (Low E*) shows general activation across the whole sample, with failure concentrated along the face diagonal. The metamaterial samples (B1-D2) show mixed mode behaviour depending on the arrangement of the two build conditions.

lattices were designed with different configurations of the two phases. These included uniform lattices, and lattices split by nodes and struts, split by horizontal layers and split by vertical pillars. The samples were based on a diamond cubic lattice structure, with a 5 mm unit cell edge length. The samples were built in both 17–4PH, which was expected to be austenitic in the Low E* condition and partially martensitic in the High E* condition, and in 316 L which was expected to be austenitic in both High E* and Low E* conditions.

Phase quantification has been previously carried out on bulk samples of additively manufactured 17-4PH built using comparable build parameters, but component geometry is a factor in the thermal strain calculation (Eq. (2)), and has been shown to have an effect on martensite content [13]. It was therefore necessary to confirm which phases were present in the 17-4PH lattice struts. Even from bulk it is challenging to prepare a suitable surface from additively build 17–4PH for XRD or EBSD without triggering unintentional deformation martensite, and this would have been exacerbated with a lattice geometry. Instead, SQUID, a magnetic technique, was used to analyse individual 'node + strut' samples which were representative of the lattice geometry but required no surface preparation. SQUID cannot distinguish between ferrite and martensite, and it was assumed that the ferromagnetic phase is martensite and the paramagnetic phase is austenite, with no ferrite present.

Low energy density (Low E*) parameters are associated with low thermal strain (Low ε^*). SQUID analysis reported that individual 'node + strut' samples built from 17 to 4PH with the Low E* parameters had $<$ 4 wt% martensite. In contrast, using high energy density (High E*) parameters, which are associated with high thermal strain (High ε^*), yielded a martensite content of $>$43 wt%. These are both slightly higher martensite fractions than reported in previous work, which could be due to geometric effects associated with the shape of the strut or the method of removal from the baseplate, however there was a significant

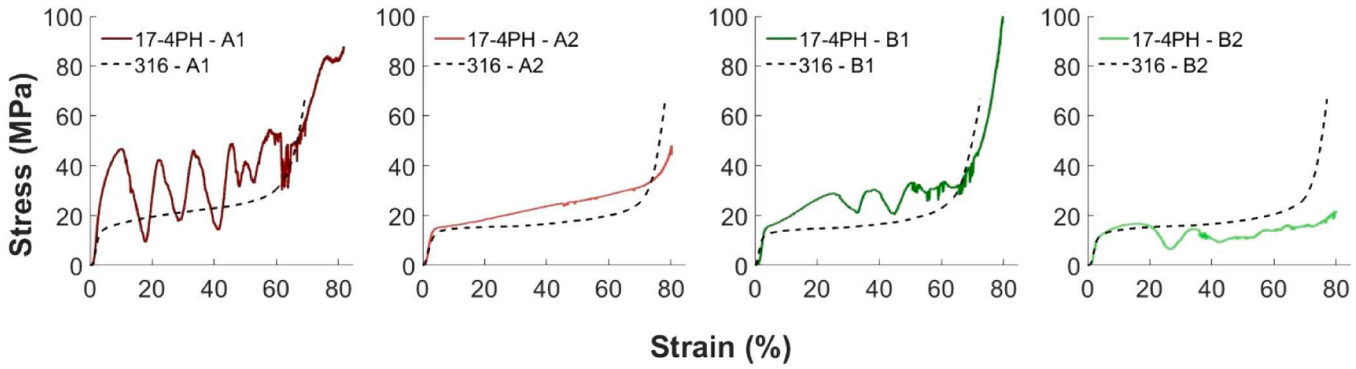

Fig. 6. Stress-strain response for Diamond Cubic lattices built in 316 L and nitrogen atomised 17–4PH. 316 L lattices all show a similar bend-dominated response irrespective of build parameters.

difference in martensite content between the two build conditions, which was the intention.

Quasi-static compression testing of the uniform 17–4PH samples showed a marked difference in mechanical response, and 2D-DIC illustrated this contextually. The A1 (High E*) sample, which had a higher martensite content, showed a stretch-dominated response with layer-by-layer collapse. In contrast, the A2 (Low E*) sample, which was almost fully austenitic, showed a bend-dominated response where the sample failed along the face diagonal. The stress strain curve for A1 shows peaks and troughs as each layer yields and collapses, while the curve for A2 shows a lower initial yield point, followed by a rising plateau as the material work hardens. The A1 behaviour is better for load-resistance, required for light-weighting in structural applications. The A2 behaviour is more suited to impact protection, where the long plateau after yield maximises the energy-absorption and protects the underlying material from damage.

The metamaterial samples (B1-D2), which had various configurations of the High E* and Low E* build conditions, showed intermediate behaviour. B1 and B2, which were split by nodes and struts, both had an initial yield point around 15 MPa, comparable with that for A2, followed by a bend-dominated plateau up to 20–30 % strain, and then a series of peaks and troughs indicative of stretch-dominated layer-by-layer collapse. C1 and C2, which had horizontal layers, had a slightly higher yield stress of 20 MPa and the work-hardening plateau extended up to 40–50 % strain before exhibiting the peaks and troughs of layer-wise collapse. D1, with martensitic pillars and austenitic infill, showed very similar behaviour to A2, but shifted to a higher stress level for the same strain; this can be seen on the DIC image where the corner pillars show a different displacement behaviour. D2, with austenitic pillars and a martensitic infill, is very similar to A1 with a primarily stretch-dominated response.

The samples built in 316 L were designed to confirm that any differences in mechanical response observed in the 17–4PH samples were due to phase content and not from other solidification effects. As expected, all four samples built in 316 L exhibited a bend-dominated austenitic response with low yield stress (~13 MPa) and a long plateau extending up to 60 % strain before the onset of densification. There was no shift from bend-dominated to stretch-dominated behaviour with build energy density in the A1 and A2 configurations, and no intermediate behaviour from the B1 and B2 configurations.

5. Conclusions

In summary, this work has demonstrated that it is possible to use laser powder-bed fusion build parameters (laser power, travel speed, hatch spacing) to adjust in-situ strain to achieve a controllable variation in martensite phase content and thereby tailor the mechanical response of structural metamaterial lattices without compositional or geometric modification. This has enabled lattices to be manufactured from the same alloy showing both stretch-dominated behaviour, suitable for light-weighed load-bearing applications, and bend-dominated behaviour, suitable for energy-absorbing impact applications. This gives a route to the design and manufacture of mechanically graded metamaterials which can display strength and ductility in different regions according to the individual component requirements. The avoidance of compositional modification enables recycling both of unused powder during the build and of the built component at end-of-life.

CRediT authorship contribution statement

Felicity S.H.B. Freeman: Data curation, Formal analysis, Funding acquisition, Investigation, Methodology, Project administration, Supervision, Validation, Visualization, Writing – original draft, Writing – review & editing. **Luke M. Jones:** Formal analysis, Investigation, Methodology, Visualization, Writing – review & editing. **Alexander D. Goodall:** Investigation, Methodology. **Hassan Ghadbeigi:** Project administration, Resources, Supervision, Validation. **Iain Todd:** Conceptualization, Methodology, Project administration, Supervision.

Declaration of Competing Interest

The authors declare that they have no known competing financial interests or personal relationships that could have appeared to influence the work reported in this paper.

Data availability

Data will be made available on request.

Funding

This work was supported by the Henry Royce Institute for Advanced Materials, funded through EPSRC grants EP/R00661X/1, EP/S019367/1, EP/P02470X/1 and EP/P025285/1, and by the EPSRC Future Manufacturing Hub in Manufacture using Advanced Powder Processes grant EP/P006566/1.

Appendix

A: Strut Thickness

Strut thickness is a key parameter in the mechanical performance of lattice structures. It was identified during preliminary work that the actual strut thickness produced is influenced by the build parameters, such that high energy density parameters, making a larger melt pool, also produce thicker struts for the same scan strategy and CAD geometry.

To enable simpler CAD modelling, this was investigated through the 'fill offset' rather than by adjusting the CAD model. The fill offset is a parameter in the build software (Autodesk Netfabb Premium 2022) which describes how closely the laser approaches the edge of the fill area for a given region of geometry. A fill offset of 0.10 mm means that the centre point of the laser will go to within 0.10 mm of the CAD definition for the edge before turning round. Dimensional accuracy of the built component relies on choosing the appropriate fill offset for the size of the melt pool, which is itself dependent on the laser power, travel speed and laser spot size.

The low E* regions were set to a fill offset of 0.00 mm, where the laser would approach right to the edge of the CAD geometry. Preliminary work indicated that the High E* parameters should use a fill offset of 0.15 mm to achieve an equivalent strut thickness to the Low E* parameters.

B: SQUID Raw Data

Table 4
Volume fraction martensite for High E* and Low E* build conditions in 17-4PH lattice geometries determined from saturation magnetisation, as an average of 5 samples.

	Sample #	Shape Correction Factor [24]	Saturation Magnetisation emu/g	Phase Fraction Martensite vol%
Low E*	1	0.90	4.3	2.7
	2	0.92	4.7	2.9
	3	0.85	6.2	3.8
	4	0.92	5.3	3.3
	5	0.86	4.2	2.6
High E*	1	0.91	77.3	47.8
	2	0.89	69.0	42.6
	3	0.90	70.0	43.2
	4	0.91	68.0	42.0
	5	0.89	10.1	43.2

C: Melt Pool Estimation

The Eagar model to predict the melt pool size is reproduced here, a MATLAB script was used to iterate the model at progressively longer time intervals until the predicted melt pool size no longer changes.

$$T - T_0 = \int_0^{t=\max} \frac{nQ}{\pi C_{psol}(4\pi a_s)^{1/2} a_s t^{1/2} + \sigma^2} \exp\left(-\frac{X^2 + Y^2 + 2Xv_t + 2i\pi t}{4a_s t + 2\sigma^2} - \frac{Z^2}{4a_s t} \right) dt \quad (5)$$

Where: C_{psol} is the specific heat capacity of the solid material, 460 J kg^{-1} K^{-1}; n is the laser efficiency; Q is the laser power; X, Y, and Z are the positions in the direction of, perpendicular to, and normal to the laser travel respectively; v_t is the laser travel velocity; σ is the standard deviation of the gaussian distribution; and $a_s = 6.32\times10{-}6$ m^2 s^{-1} is the thermal diffusivity. The last term is approximately $2.5 \times 10{-}9$ m^2 and the beam radius term, σ^2, around $1.2 \times 10{-}9$ m^2. Here the dominant term $2a_{s,t} + \sigma^2$ describes the distance over which heat is transferred which is a function of the thermal diffusivity in the solid $2a_{s,t}$ the time t and the beam radius σ. Readers are referred to [20] for further details regarding melt pool size calculations.

D: Nominal chemical composition

The chemical composition of samples built with the high and low energy parameters were confirmed to be almost identical and within the expected range from the manufacturer for the power via inductively coupled plasma (ICP) spectroscopy and LECO elemental analysis for Carbon and Oxygen.

Element	High E* (%)	Low E* (%)	Element	High E* (%)	Low E* (%)
Al	<0.05	<0.05	P	0.006	0.005
B	<0.02	<0.02	Si	0.69	0.64
Co	0.07	0.06	Sn	<0.02	<0.02
Cr	16.24	16.10	Ta	<0.02	<0.02
Cu	4.00	4.42	Ti	<0.02	<0.02
Fe	73.80	73.56	V	0.06	0.06
Mn	0.33	0.42	W	0.02	0.02
Mo	0.08	0.07	C	0.04	0.05
Nb	0.28	0.26	O	0.021	0.031
Ni	4.36	4.30			

E: Porosity

Density was measured using the Archimedes principle revealing an approximate 0.2 g/cm^3 decrease for High E* samples; sectioning revealed some porosity in these samples. This increases the effective stress on the struts and nodes, thus further verifying the difference is due to the architected phase difference because the load bearing capacity of the high energy samples was greater than that of Low E* samples.

Sample	Density (g/cm^3)	Sample	Density (g/cm^3)
High E* 1	7.682	Low E* 1	7.853
High E* 2	7.685	Low E* 2	7.808

Fig. E1 shows pores identified by focus variation on samples sectioned using wire EDM. The pores have been highlighted for ease of identification by the reader. Using ImageJ [30] the High E* Sample was found to be 96.457 % dense and the Low E* sample 98.359 % dense.

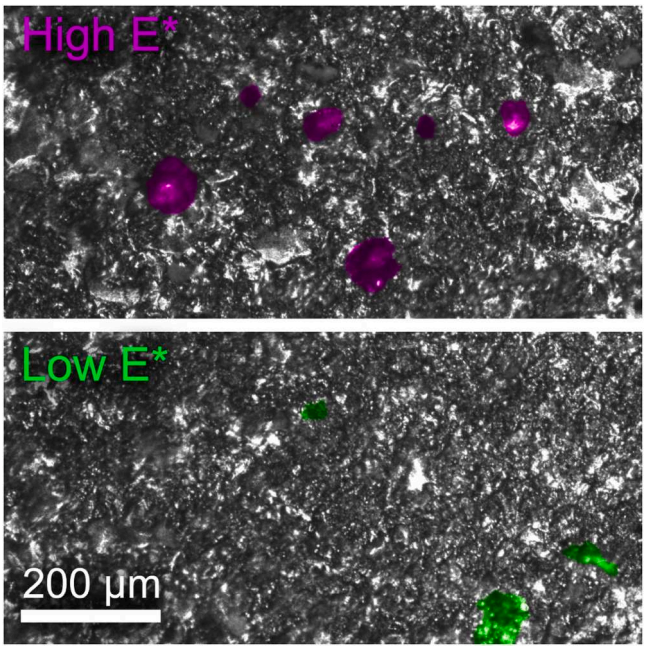

Fig. E1. Pores identified in sectioned samples.

References

[1] A. du Plessis, S. Mohammad Javad Razavi, M. Benedetti, S. Murchio, M. Leary, M. Watson, D. Bhate, F. Berto, Properties and applications of additively manufactured metallic cellular materials: a review, Prog. Mater Sci. 125 (2021), 100918, https://doi.org/10.1016/j.pmatsci.2021.100918.

[2] X. Zhou, L. Ren, Z. Song, G. Li, J. Zhang, B. Li, Q. Wu, W. Li, L. Ren, Q. Liu, Advances in 3D/4D printing of mechanical metamaterials: from manufacturing to applications, Compos. Part B Eng. 254 (2023), 110585, https://doi.org/10.1016/j.compositesb.2023.110585.

[3] D. Raabe, C.C. Tasan, E.A. Olivetti, Strategies for improving the sustainability of structural metals, Nature 575 (2019) 64–74, https://doi.org/10.1038/s41586-019-1702-5.

[4] D.C. Hofmann, J. Kolodziejska, S. Roberts, R. Otis, R.P. Dillon, J.O. Suh, Z.K. Liu, J. P. Borgonia, Compositionally graded metals: a new frontier of additive manufacturing, J. Mater. Res. 29 (2014) 1899–1910, https://doi.org/10.1557/jmr.2014.208.

[5] Z. Ozdemir, E. Hernandez-Nava, A. Tyas, J.A. Warren, S.D. Fay, R. Goodall, I. Todd, H. Askes, Energy absorption in lattice structures in dynamics: experiments, Int. J. Impact Eng. 89 (2016) 49–61, https://doi.org/10.1016/J.IJIMPENG.2015.10.007.

[6] M. Benedetti, A. du Plessis, R.O. Ritchie, M. Dallago, S.M.J. Razavi, F. Berto, Architected cellular materials: a review on their mechanical properties towards fatigue-tolerant design and fabrication, Mater. Sci. Eng. R Rep. 144 (2021), 100606, https://doi.org/10.1016/j.mser.2021.100606.

[7] J. Feng, B. Liu, Z. Lin, J. Fu, Isotropic octet-truss lattice structure design and anisotropy control strategies for implant application, Mater. Des. 203 (2021), 109595, https://doi.org/10.1016/J.MATDES.2021.109595.

[8] M. Dharmaraj, K.V. Satheesh kumar, C. Sridhar, Crashworthiness unit cell design investigation for energy absorption analysis, Mater. Today Proc. 50 (2022) 1282–1290, https://doi.org/10.1016/j.matpr.2021.08.151.

[9] L. Zhao, S.M. Ryan, J.K. Ortega, S. Ha, K.W. Sharp, J.K. Guest, K.J. Hemker, T. P. Weihs, Experimental investigation of 3D woven Cu lattices for heat exchanger applications, Int. J. Heat Mass Transf. 96 (2016) 296–311, https://doi.org/10.1016/j.ijheatmasstransfer.2015.12.059.

[10] C. Yan, L. Hao, A. Hussein, P. Young, D. Raymont, Advanced lightweight 316L stainless steel cellular lattice structures fabricated via selective laser melting, Mater. Des. 55 (2014) 533–541, https://doi.org/10.1016/j.matdes.2013.10.027.

[11] W. van Grunsven, E. Hernandez-Nava, G. Reilly, R. Goodall, Fabrication and mechanical characterisation of titanium lattices with graded porosity, Metals 4 (2014) 401–409, https://doi.org/10.3390/met4030401.

[12] J.H. Bastek, S. Kumar, B. Telgen, R.N. Glaesener, D.M. Kochmann, Inverting the structure–property map of truss metamaterials by deep learning, Proc. Natl. Acad. Sci. U. S. A. 119 (2022), https://doi.org/10.1073/pnas.211150511.

[13] F. Freeman, A. Lincoln, J. Sharp, A. Lambourne, I. Todd, Exploiting thermal strain to achieve an *in-situ* magnetically graded material, Mater. Des. 161 (2019) 14–21, https://doi.org/10.1016/j.matdes.2018.11.011.

[14] F. Freeman, J. Sharp, J. Xi, I. Todd, Influence of solidification cell structure on the martensitic transformation in additively manufactured steels, Addit. Manuf. 30 (2019), 100917, https://doi.org/10.1016/j.addma.2019.100917.

[15] L. Facchini, N. Vicente Jr, I. Lonardelli, E. Magalini, P. Robotti, A. Molinari, Metastable austenite in 17–4 precipitation-hardening stainless steel produced by selective laser melting, Adv. Eng. Mater. (2010) 184–188.

[16] Sandmeyer Steel, Alloy 17-4 PH Precipitation Hardening Specification Sheet, Sandmeyer Steel Company. (2016). https://www.sandmeyersteel.com/17-4PH.html#PhysicalProperties . (accessed December 13, 2023).

[17] M. Thomas, G.J. Baxter, I. Todd, Normalised model-based processing diagrams for additive layer manufacture of engineering alloys, Acta Mater. 108 (2016) 26–35, https://doi.org/10.1016/j.actamat.2016.02.025.

[18] T. Mukherjee, J.S. Zuback, A. De, T. Debroy, Printability of alloys for additive manufacturing, Sci. Rep. 6 (2016), https://doi.org/10.1038/srep19717.

[19] J. Trapp, A.M. Rubenchik, G. Guss, M.J. Matthews, In situ absorptivity measurements of metallic powders during laser powder-bed fusion additive manufacturing, Appl. Mater. Today 9 (2017) 341–349, https://doi.org/10.1016/j.apmt.2017.08.006.

[20] F. Freeman, Structuring Difference: The Additive Manufacture of Spatially & Functionally Differentiated Microstructures, University of Sheffield, 2018. http://etheses.whiterose.ac.uk/22742/ (accessed September 3, 2019).

[21] Q. Guo, C. Zhao, M. Qu, L. Xiong, L.I. Escano, S.M.H. Hojjatzadeh, N.D. Parab, K. Fezzaa, W. Everhart, T. Sun, L. Chen, *In-situ* characterization and quantification of melt pool variation under constant input energy density in laser powder bed fusion additive manufacturing process, Addit. Manuf. 28 (2019) 600–609, https://doi.org/10.1016/j.addma.2019.04.021.

[22] B.D. Cullity, C.D. Graham, Introduction to Magnetic Materials, IEEE/Wiley, 2009.

[23] S.S.M. Tavares, J.M. Pardal, T.R.B. Martins, M.R. da Silva, Influence of sulfur content on the corrosion resistance of 17-4PH stainless steel, J. Mater. Eng. Perform. 26 (2017) 2512–2519, https://doi.org/10.1007/s11665-017-2693-8.

[24] C.O. Amorim, F. Mohseni, R.K. Dumas, V.S. Amaral, J.S. Amaral, A geometry-independent moment correction method for the MPMS3 SQUID-based magnetometer, Meas. Sci. Technol. 32 (2021), https://doi.org/10.1088/1361-6501/ac0d23.

[25] S. Takaki, K. Fukunaga, J. Syarif, T. Tsuchiyama, Effect of grain refinement on thermal stability of metastable austenitic steel, Mater. Trans. 45 (2004) 2245–2251, https://doi.org/10.2320/matertrans.45.2245.
[26] H.S. Yang, H.K.D.H. Bhadeshia, Austenite grain size and the martensite–start temperature, Scr. Mater. 60 (2009) 493–495, https://doi.org/10.1016/j.scriptamat.2008.11.043.
[27] H.K. Rafi, D. Pal, N. Patil, T.L. Starr, B.E. Stucker, Microstructure and mechanical behavior of 17-4 precipitation hardenable steel processed by selective laser melting, J. Mater. Eng. Perform. 23 (2014) 4421–4428, https://doi.org/10.1007/s11665-014-1226-y.
[28] AK Steel Corporation, Specification for 17-4PH stainless steel, Datasheet 172888 (2007) 1–2. https://www.aksteel.nl/files/downloads/172888_armco_17-4_ph_pdb_euro_final_secured_89.pdf . (accessed 13 December 2023).
[29] S. Cheruvathur, E.A. Lass, C.E. Campbell, Additive manufacturing of 17-4 PH stainless steel: post-processing heat treatment to achieve uniform reproducible microstructure, JOM 68 (2016) 930–942, https://doi.org/10.1007/s11837-015-1754-4.
[30] C.A. Schneider, W.S. Rasband, K.W. Eliceiri, NIH image to ImageJ: 25 years of image analysis, Nat. Methods 9 (7) (2012) 671–675, https://doi.org/10.1038/nmeth.2089.